

# Computer modeling investigation of MgV<sub>2</sub>O<sub>4</sub> for Mg-ion batteries

Kuganathan, N., Davazoglou, K. & Chroneos, A.

Author post-print (accepted) deposited by Coventry University's Repository

**Original citation & hyperlink:**

Kuganathan, N, Davazoglou, K & Chroneos, A 2020, 'Computer modeling investigation of MgV<sub>2</sub>O<sub>4</sub> for Mg-ion batteries', Journal of Applied Physics, vol. 127, no. 3, 035106.

<https://dx.doi.org/10.1063/1.5139114>

DOI 10.1063/1.5139114

ISSN 0021-8979

ESSN 1089-7550

Publisher: American Institute of Physics

**This article may be downloaded for personal use only. Any other use requires prior permission of the author and AIP Publishing. This article appeared in Kuganathan, N, Davazoglou, K & Chroneos, A 2020, 'Computer modeling investigation of MgV<sub>2</sub>O<sub>4</sub> for Mg-ion batteries', Journal of Applied Physics, vol. 127, no. 3, 035106. and may be found at <https://dx.doi.org/10.1063/1.5139114>**

**Copyright © and Moral Rights are retained by the author(s) and/ or other copyright owners. A copy can be downloaded for personal non-commercial research or study, without prior permission or charge. This item cannot be reproduced or quoted extensively from without first obtaining permission in writing from the copyright holder(s). The content must not be changed in any way or sold commercially in any format or medium without the formal permission of the copyright holders.**

**This document is the author's post-print version, incorporating any revisions agreed during the peer-review process. Some differences between the published version and this version may remain and you are advised to consult the published version if you wish to cite from it.**

# Computer Modelling Investigation of $\text{MgV}_2\text{O}_4$ for Mg-ion batteries

Navaratnarajah Kuganathan <sup>1,2\*</sup>, Konstantinos Davazoglou<sup>3</sup>, Alexander Chroneos <sup>1,2</sup>

<sup>1</sup>Department of Materials, Imperial College London, London, SW7 2AZ, United Kingdom

<sup>2</sup>Faculty of Engineering, Environment and Computing, Coventry University, Priory Street, Coventry CV1 5FB, United Kingdom

<sup>3</sup>Department of Informatics and Telecommunications, National and Kapodistrian University of Athens, GR 15784 Athens, Greece

---

## Abstract

$\text{MgV}_2\text{O}_4$  is a vanadium spinel considered for rechargeable magnesium ion batteries. Its defect chemistry, solution of dopants and the diffusion of Mg-ions are investigated using advanced atomistic modelling techniques. The energetically most favourable defect is Mg-V anti-site cluster (0.53 eV/defect) assuming that a small percentage of  $\text{Mg}^{2+}$  and  $\text{V}^{3+}$  ions would exchange their positions particularly at higher temperatures. Reaction energies for the loss of MgO *via* MgO Schottky and the formation of Mg vacancies *via* Mg Frenkel are calculated to be 5.13 eV/defect and 5.23 eV/defect suggesting that the concentrations of these two defects will be not be significant. The most favourable diffusion mechanism of Mg ions is a three dimensional pathway, where the activation energy of migration is 0.52 eV. Formation of Mg interstitials and O vacancies can be facilitated by doping with  $\text{Co}^{2+}$  at the V site in  $\text{MgV}_2\text{O}_4$ . The electronic structures of the favourable dopants calculated using density functional theory are discussed.

**Keywords:**  $\text{MgV}_2\text{O}_4$ ; defects; diffusion; dopants; computer modelling

\*Corresponding author's email address: n.kuganathan@imperial.ac.uk

## 1. Introduction

The urgent demand for the further development of clean energy storage devices with novel functionalities and pronounced storage capacity led the community to investigate alternative materials for application to lithium ion batteries. Sodium (Na)-ion batteries are promising candidates as they are cheaper, Na is abundant and they can be safer [1-3]. For a battery, high energy density storage capacity is important and this can be achieved by utilizing battery materials based on multivalent charge carrier ions.

Rechargeable batteries based on manganese (Mg)-ions have attracted considerable attention as potential candidates for next-generation energy storage systems mainly due to their high capacity (both gravimetric and volumetric) provided by Mg-based electrode materials [4-6]. Mg is abundant, non-toxic and it is relatively safe to use due to its higher melting temperature as compared to lithium (Li). The size of  $Mg^{2+}$  ion is similar to that of  $Li^+$  one but the strong ionic interaction of  $Mg^{2+}$  ions with host lattices makes the intercalation harder. Though this issue can be partly resolved by reducing the size of the cathode particle and increasing the shielding of  $Mg^{2+}$  ions inserted, a limited number of cathode materials including vanadium oxides (e.g.  $V_2O_5$ ), manganese oxides (e.g.  $MnO_2$ ) and silicates (e.g.  $MgFeSiO_4$ ) have been previously considered [7-11].

Vanadium (V) based oxide materials have been considered appropriate for use in a vast variety of energy related applications including energy storage devices due to the ability of vanadium to possess variable oxidation states [12-15].  $MgV_2O_4$  is a cubic spinel based oxide that has been recently introduced as a candidate cathode material for Mg-ion batteries. Lee *et al.* [16] performed a systematic nuclear magnetic resonance (NMR) and density functional theory (DFT) study to unveil the magnetic ordering in  $MgV_2O_4$ ,  $Mg_6MnO_8$  and  $MgCr_2O_4$ . Electrochemical activity arising from defects and Mg-ion diffusion in the as-prepared and cycled structures is, however, not available.

In a recent study Shrivastava *et al.* [17], inserted suitable dopants, such as  $Cr^{3+}$  and  $Fe^{3+}$ , into the V site in  $MgV_2O_4$  and examined the impact on structural, catalytic and magnetic properties. In previous theoretical studies of our group [18-24], a variety of oxide materials including Mg based oxides such as  $MgTiO_3$  and  $Mg_6MnO_8$  was examined regarding their structural and electronic properties as well as their catalytic activity. We concluded that theoretical simulations based on classical potentials can be useful in the future experimental studies providing

information regarding defect structures, diffusion properties and solution of promising dopants at the V and Mg sites.

Here we use atomistic simulation to identify the key defects in  $\text{MgV}_2\text{O}_4$ , as well as promising dopants that could improve the material properties and the Mg-ion transport. Electronic structures of doped-configurations calculated using DFT simulations are also discussed.

## 2. Computational Methods

The General Utility Lattice Program (GULP) (version 3.4.1) was used to run simulations based on force field methods [25, 26]. This program enabled us to perform geometry optimizations and calculate defect energies, solution energies for dopants and Mg-ion migration pathways. Ionic interactions were considered using long range (Coulombic) and short-range (Pauli repulsion and van der Waals attraction) interactions. The latter were modelled using Buckingham potentials. The Mott-Littleton method [27] as implemented in the GULP code was used to model point defects. Polarization of ions was treated using the core-shell model.

Electronic structure calculations were performed to examine the impact of favourable dopants on the electronic structure of  $\text{MgV}_2\text{O}_4$  using the spin-polarized DFT code VASP (Vienna ab initio simulation program) [28, 29]. This code uses plane wave basis sets and projected augmented wave (PAW) potentials. We used a plane wave basis set with a cut-off of 500 eV. Defect calculations were performed using a supercell containing 56 atoms. Monkhorst pack k-points ( $8 \times 8 \times 8$  k points for bulk and defective supercell) were used [30]. Exchange correlation was included within the generalized gradient approximation (GGA) as parameterized by Perdew, Burke, and Ernzerhof (PBE) [31]. Conjugate gradient algorithm was used to optimize the atomic positions and the lattice parameters of the cell [32]. Attractive interactions arising from dispersion were modelled using a semi-empirical DFT-D3 scheme included in the VASP code [33]. Isobaric parameters were used to calculate the formation and migration energies. In our previous work, we have discussed in detail the thermodynamic relations associated with isobaric parameters [34-38].

## 3. Results and Discussions

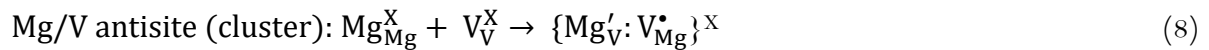
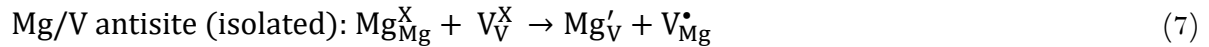
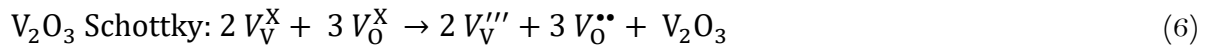
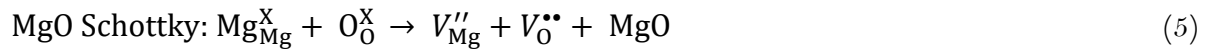
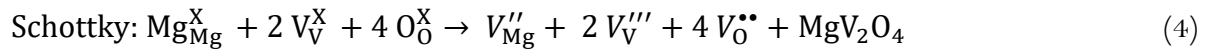
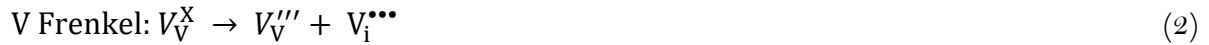
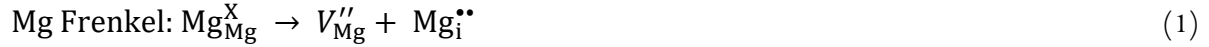
### 3.1. Modelling of crystal structure of $\text{MgV}_2\text{O}_4$

MgV<sub>2</sub>O<sub>4</sub> crystallizes in a cubic spinel structure with space group  $Fd\bar{3}m$  (no. 227). Its experimental lattice constant was reported to be 8.3850 Å [39]. In this crystal structure, Mg<sup>2+</sup> and V<sup>3+</sup> ions form tetrahedral and octahedral units, respectively, through corners sharing (refer to Figure 1). We used previously published Buckingham potentials (refer to Table S1 in the supplementary information) and standard PAW potentials in GULP and VASP respectively to reproduce the experimental lattice parameter of the bulk MgV<sub>2</sub>O<sub>4</sub>. Table 1 reports the experimental and calculated values of lattice parameters together with the error percentage. The values calculated using both methods reproduce the experimental structure very well with the error margin being less than 0.70 %.

### 3.2. Intrinsic defect properties

In this section, we discuss the three key defect processes namely Schottky, Frenkel and anti-site. In order to calculate the Schottky and Frenkel defect energies, it was necessary to calculate the energies of point defects (vacancies and interstitials). Figure 2 shows the schematic diagrams of point defects (vacancy, interstitial) and anti-site defect.

There are eight intrinsic defect processes exhibited by MgV<sub>2</sub>O<sub>4</sub>; these processes are outlined in equations (1-8) using the Kröger-Vink notation [40].



Calculations show that the formation of Mg-V anti-site defect cluster is energetically favourable (0.53 eV/defect). In this defect process, Mg<sup>2+</sup> and V<sup>3+</sup> undergo a simultaneous exchange of their atomic positions. Many experimental and theoretical studies [18-22,41-47] have discussed

analogous defects in detail. In the isolated form of anti-site defect both  $\text{Mg}'_{\text{V}}$  and  $\text{V}^{\bullet}_{\text{Mg}}$  are calculated independently and their energies are combined. The energy difference between the clustered and isolated forms is the binding energy ( $-0.31$  eV). The negative value indicates that isolated charged defects are not stable and prefer to cluster. The strength of binding depends on the charges on the isolated defects. For example, in our previous study, the binding energy was  $-1.36$  eV for the attraction between  $\text{Mg}''_{\text{Mn}}$  and  $\text{Mn}^{\bullet\bullet}_{\text{Mg}}$  in  $\text{Mg}_6\text{MnO}_8$ . Defect energies of Mg Frenkel, MgO Schottky, Schottky and  $\text{V}_2\text{O}_3$  Schottky are between  $5.13$  eV and  $5.36$  eV suggesting that these defect processes are not favoured at room temperature and would only take place at high temperatures. Oxygen and vanadium Frenkel energies are calculated to be  $6.26$  eV and  $6.98$  eV, respectively, implying low concentrations of oxygen and vanadium vacancies at room temperature.

### 3.3. Mg-ion diffusion

We furthermore calculated Mg-ion migration pathways and their activation energies as they are important for intercalation and de-intercalation processes. Force field atomistic simulations were used to calculate the Mg vacancy migration pathways and the respective activation energies of migration. We identified Mg local hops (refer to arrows in figure 3 a) with the Mg-Mg distances being  $3.62$  Å. The activation energy of migration for this local hop is  $0.52$  eV. Mg-ion migration path calculated for this local hop is shown in Figure 3a (refer to yellow atoms). Three-dimensional long range pathways were constructed by connecting Mg local hops as shown in Figure 3 a. Activation energy for this long-range migration would be  $0.52$  eV as there is only one local hop present. The results show that ionic conductivity in this material is relatively high and the activation energy calculated for Mg-ion migration is relatively low compared to those found in other oxide based Mg-ion battery materials [refer to Table 3][21,48-51]. Previous theoretical study shows that  $\text{MgA}_2\text{B}_4$  ( $A=\text{Y}$  or  $\text{Sc}$  and  $B = \text{S}$  or  $\text{Se}$  or  $\text{Te}$ ) compounds exhibit lower activation energies ( $0.30$ - $0.40$  eV) than that calculated in the oxide based Mg materials as reported in Table 3 [52].

### 3.4. Solution of dopants

As substitution with dopants represents an effective way towards improving an electrode performance, we next investigated the incorporation of a range of cations in  $\text{MgV}_2\text{O}_4$  using force field method and identified the most favourable dopants hence offering guidelines for the formation and experimental study of potential electrode materials. Here we discuss the doping mechanism considering solution energy, cation size and local structure.

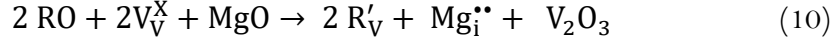
### ***3.4.1. Divalent dopants***

The impact of divalent doping ( $\text{R} = \text{Ni, Co, Zr, Fe, Ca, Sr}$  and  $\text{Ba}$ ) at the  $\text{Mg}$  site is first considered. The doping procedure is thoroughly described by the following equation:



In Figure 4, the calculated solution enthalpies are reported. Exoergic solution enthalpies are noted for  $\text{Zn}^{2+}$ ,  $\text{Fe}^{2+}$  and  $\text{Ca}^{2+}$  which implies that doping with these elements is highly favourable and such material systems should be investigated experimentally. The possible formula of the doped composition can be represented as  $\text{Mg}_{1-x}\text{R}_x\text{V}_2\text{O}_4$  ( $\text{R} = \text{Zn, Fe}$  and  $\text{Ca}$ ). The ionic radius of  $\text{Mg}^{2+}$  in the tetrahedral coordination is  $0.57 \text{ \AA}$ . Amongst favourable dopants  $\text{Zn}^{2+}$ , with an ionic radius that is close to that of  $\text{Mg}^{2+}$ , is considered as the most preferable one (solution enthalpy is  $-0.24 \text{ eV}$ ). As the ionic radii of  $\text{Fe}^{2+}$  and  $\text{Ca}^{2+}$  are slightly larger than that of  $\text{Mg}^{2+}$ , their solution energies are slightly higher. Both  $\text{Ni}^{2+}$  and  $\text{Co}^{2+}$  exhibit endoergic solution enthalpies though their ionic radii are closer to that of  $\text{Mg}^{2+}$ . There is a gradual increase in the solution enthalpy with ionic radius from  $\text{Sr}^{2+}$  to  $\text{Ba}^{2+}$ . As high solution enthalpies are calculated for  $\text{Sr}^{2+}$  and  $\text{Ba}^{2+}$ , doping should be carried out at high temperatures.

Thereafter, we considered the doping of divalent cations at the  $\text{V}$  site. Two different possible mechanisms are suggested (refer to Eqns 10 & 11). In the first mechanism (equation 10),  $\text{Mg}$  interstitials are introduced as charge compensation defects. This process can increase the amount of  $\text{Mg}$  required for the efficient intercalation/de-intercalation process. The solution energies for this process are shown in Figure 5a. The lowest solution enthalpy is calculated for  $\text{Co}^{2+}$ . Solution energies of  $\text{Ni}^{2+}$ ,  $\text{Co}^{2+}$ ,  $\text{Zn}^{2+}$  and  $\text{Fe}^{2+}$  are endoergic ( $\sim 3.30 \text{ eV}$ ) and close to each other suggesting that significant energy should be provided for this process. Solution enthalpy increases with the cationic radius from  $\text{Ca}^{2+}$  to  $\text{La}^{3+}$ .



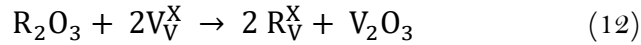
In the second process, oxygen vacancies are generated to compensate charge introduced by the doping. Equation 11 explains this process and solution enthalpies are shown in Figure 5b.



Similar trend to that discussed above for the solution enthalpy is observed for the process of Mg interstitials. Solution enthalpies are almost the same and differs only by  $\sim 0.10$  eV. This result indicates that the dopants  $Ni^{2+}$ ,  $Co^{2+}$ ,  $Zr^{2+}$  and  $Fe^{2+}$  can be tested experimentally though their solutions are high.

### 3.4.2. Trivalent dopants

Finally, trivalent dopants ( $R=Al^{3+}$ ,  $Ni^{3+}$ ,  $Co^{3+}$ ,  $Cr^{3+}$ ,  $Ga^{3+}$ ,  $Fe^{3+}$ ,  $Mn^{3+}$ ,  $Sc^{3+}$ ,  $Y^{3+}$  and  $La^{3+}$ ) were considered at the V site. Charge compensation defect was not necessary in this process as both V and dopants are in +3 charge state as explained in the equation 12.



Solution enthalpies are reported in Figure 6. Previous experimental studies have also considered the doping with trivalent cations such as  $Al^{3+}$ ,  $Cr^{3+}$  and  $Fe^{3+}$  at the V site. Mamiya *et al.* [53] used solid state reaction method to synthesize Al-doped  $MgV_2O_4$  and examine its structural and magnetic properties compared to that of  $MgV_2O_4$ . In a different experimental study, Shrivastava *et al.* [17] studied the effect of doping of  $Cr^{3+}$  and  $Fe^{3+}$  at the vanadium site in  $MgV_2O_4$ . Here we calculate the solution enthalpies for different trivalent dopants (including  $Al^{3+}$ ,  $Cr^{3+}$  and  $Fe^{3+}$ ) to predict the most promising dopants that should be examined experimentally. Calculations show that  $Al^{3+}$ ,  $Ni^{3+}$ ,  $Co^{3+}$  and  $Cr^{3+}$  exhibit exoergic solution enthalpies and thus they are promising. This is in line with the experimental studies regarding the doping of  $Al^{3+}$  and  $Cr^{3+}$ . Solution enthalpies of  $Ga^{3+}$  and  $Fe^{3+}$  are 0.01 eV and 0.14 eV respectively suggesting that they should also be considered for experimental verification. Solution enthalpy increases with ionic radius from  $Mn^{3+}$  to  $La^{3+}$ . High positive solution enthalpy calculated for  $La^{3+}$  shows that doping with this cation is unlikely to carry out experimentally.

### 3.5. Electronic structures of doped- $MgV_2O_4$ composites

DFT simulations were performed to examine the electronic structures of both defect-free and doped structures. Here, we consider the favourable dopants as reported in section 3.4 for discussion.

The electronic structure of  $\text{MgV}_2\text{O}_4$  has been previously discussed by Pandey [54]. Non-magnetic (NM) structure is 0.65 eV/f.u (f.u=formula unit) higher in energy than ferromagnetic structure (FM) in his study. This is in agreement with the present simulation. Here, the trend is the same and the energy difference is 0.55 eV/f.u. Calculated density of states (DOS) exhibits metallic behavior as observed in the previous simulations [54]. These considered GGA and GGA+U flavors and in both cases magnetic ground state was observed. Anti-ferromagnetic (AFM) configuration created a small band gap of 0.16 eV. Here we considered only FM configurations in all cases as the purpose of this section is only to consider how dopants change the electronic structure of the  $\text{MgV}_2\text{O}_4$ .

Divalent dopants at the Mg site are first discussed. Figure 7 shows the doped configurations, DOSs (both total and atom) and charge densities around the doped atoms. In the Zn-doped configuration, Zn-O bond distances differ only by  $\sim 0.01$  Å from Mg-O bond distances (refer to Figure 7b). This is reflected in the low value of solution enthalpy calculated for Zn ( $-0.24$  eV). As the deviation in the bond distances increases from Fe to Ca, solution enthalpy also increases from  $-0.16$  eV to  $-0.07$  eV respectively.

The Fermi energy is slightly reduced upon doping. In the case of Zn, its  $d$  states are further away from the Fermi level. This can be due to the complete  $d^{10}$  configuration with non-magnetic nature. This is supported by the charge density around Zn (refer to Figure 7l). Doping with Fe at the Mg site introduces  $d$  states near the Fermi level and perturbs the lattice as shown in the charge density plot (refer to Figure 7m). The  $p$  states of Ca appear near the Fermi level and valence band reflecting this effect in the charge density plot.

Next we considered the  $\text{Co}^{2+}$  occupying the V site. Co-O bond distances are slightly longer than V-O bond distances. This is due to the higher strength of the  $\text{V}^{3+}\text{-O}^{2-}$  bond compared to the  $\text{Co}^{2+}\text{-O}^{2-}$  one. Co-doping introduces a reduction in the Fermi energy by 0.19 eV. The Fermi energy level is slightly altered (refer to Figure 8d) and this can be due to the cation charge mismatch. Figure 8e shows additional states arising from Co doping between 4.50-6.00 eV. As

Co<sup>2+</sup> doping at the V<sup>3+</sup> site introduces an electron in the lattice, there is probably a charge delocalization within the lattice as shown in Figure 8f.

Finally, the structure and electronic properties of Al-doped MgV<sub>2</sub>O<sub>4</sub> are discussed. Even though, Al and V exhibit +3 charge in the lattice, Al-O bond lengths are shorter than the V-O bond ones due to smaller ionic radius of Al<sup>3+</sup> compared to V<sup>3+</sup> in an octahedral coordination. Figure 9 shows the chemical environment of V and Al in defect-free and Al-doped MgV<sub>2</sub>O<sub>4</sub> lattice respectively, DOSs and constant charge density distribution arising from Al-doping. The Fermi energy increases only by 0.04 eV upon Al doping. States arising from Al-doping are noted between 0.00 and -2.00 eV and these mainly consist of *s* and *p* orbitals of Al. Charge density associated with additional states are mainly localized around the Al atom.

#### 4. Conclusions

The present computational study examined the formation of key defect processes, Mg-ion diffusion pathways and the promising dopants at the Mg and V sites in MgV<sub>2</sub>O<sub>4</sub>. The Mg-V anti-site defect was found to be the most energetically favourable one. Mg-ion diffusion in this material is calculated to be three-dimensional with an activation energy of migration of 0.52 eV implying higher Mg-ion conductivity in MgV<sub>2</sub>O<sub>4</sub> than that calculated in other Mg-ion based battery materials. The amount of Mg in the form of Mg interstitials and O vacancies can be increased by doping with Co<sup>2+</sup> at the V site. Promising isovalent dopants at the V site are calculated to be Al<sup>3+</sup>, Ni<sup>3+</sup>, Co<sup>3+</sup> and Cr<sup>3+</sup> in agreement with recent experimental reports on the successful synthesis of Al and Cr-doped MgV<sub>2</sub>O<sub>4</sub>. Electronic structure unveiled the difference in the electronic properties between un-doped and the doped configurations. Analysis of the point defects and defect processes using thermodynamic models should be considered in future work [55,56].

#### Conflicts of interest

The authors declare that there is no competing financial interest.

#### Supplementary Materials

See the supplementary material for the Buckingham potentials used in the classical simulation of the current study.

## Funding

This research was financially supported by the European Union's H2020 Programme under Grant Agreement no. 824072–HARVESTORE

**Acknowledgement.** Computational facilities and support were provided by High Performance Computing Centre at Imperial College London.

## References

- 1 J.-Y. Hwang, S.-T. Myung, and Y.-K. Sun, *Chemical Society Reviews* **46**, 3529 (2017).
- 2 N. Yabuuchi, K. Kubota, M. Dahbi, and S. Komaba, *Chemical Reviews* **114**, 11636 (2014).
- 3 M. S. Islam and C. A. J. Fisher, *Chemical Society Reviews* **43**, 185 (2014).
- 4 M. Mao, T. Gao, S. Hou, and C. Wang, *Chemical Society Reviews* **47**, 8804 (2018)
- 5 M. M. Huie, D. C. Bock, E. S. Takeuchi, A. C. Marschilok, and K. J. Takeuchi, *Coordination Chemistry Reviews* **287**, 15 (2015).
- 6 J. Muldoon, C. B. Bucur, and T. Gregory, *Chemical Reviews* **114**, 11683 (2014).
- 7 S. H. Lee, R. A. DiLeo, A. C. Marschilok, K. J. Takeuchi, and E. S. Takeuchi, *ECS Electrochemistry Letters* **3**, A87 (2014).
- 8 Y. Li, Y. Nuli, J. Yang, T. Yiliner, and J. Wang, *Chinese Science Bulletin* **56**, 386 (2011).
- 9 Z.-D. Huang, T. Masese, Y. Orikasa, T. Mori, T. Minato, C. Tassel, Y. Kobayashi, H. Kageyama, and Y. Uchimoto, *Journal of Materials Chemistry A* **2**, 11578 (2014).
- 10 Z. Feng, J. Yang, Y. NuLi, and J. Wang, *Journal of Power Sources* **184**, 604 (2008).
- 11 S. Gu, C.-T. Hsieh, M. M. Huq, J.-P. Hsu, Y. Ashraf Gandomi, and J. Li, *Journal of Solid State Electrochemistry* **23**, 1399 (2019).
- 12 L. Li, Y. Zheng, S. Zhang, J. Yang, Z. Shao, and Z. Guo, *Energy & Environmental Science* **11**, 2310 (2018).
- 13 P. Liu, K. Zhu, Y. Gao, H. Luo, and L. Lu, *Advanced Energy Materials* **7**, 1700547 (2017).
- 14 C. F. Armer, J. S. Yeoh, X. Li, and A. Lowe, *Journal of Power Sources* **395**, 414 (2018).
- 15 X.-M. Shi, X.-Y. Lang, L. Gu, Z. Wen, M. Zhao, and Q. Jiang, *Nature Communications* **9**, 1375 (2018).
- 16 J. Lee, I. D. Seymour, A. J. Pell, S. E. Dutton, and C. P. Grey, *Physical Chemistry Chemical Physics* **19**, 613 (2017).
- 17 V. Shrivastava, V. K. Tripathi, and R. Nagarajan, *Dalton Transactions* **48**, 16661 (2019).

- 18 N. Kuganathan and A. Chroneos, *Scientific Reports* **8**, 14669 (2018).
- 19 N. Kuganathan, A. Kordatos, and A. Chroneos, *Scientific Reports* **8**, 12621 (2018).
- 20 R. Kaushalya, P. Iyngaran, N. Kuganathan, and A. Chroneos, *Energies* **12**, 3094 (2019).
- 21 N. Kuganathan, P. Iyngaran, R. Vovk, and A. Chroneos, *Scientific Reports* **9**, 4394 (2019).
- 22 N. Kuganathan, E. I. Gkanas, and A. Chroneos, *Energies* **12**, 3213 (2019).
- 23 R. W. Grimes, G. Busker, M. A. McCoy, A. Chroneos, J. A. Kilner, and S.-P. Chen, *Berichte der Bunsengesellschaft für physikalische Chemie* **101**, 1204 (1997).
- 24 E. E. Jay, M. J. D. Rushton, A. Chroneos, R. W. Grimes, and J. A. Kilner, *Physical Chemistry Chemical Physics* **17**, 178 (2015).
- 25 J. D. Gale and A. L. Rohl, *Molecular Simulation* **29**, 291 (2003).
- 26 J. D. Gale, *Journal of the Chemical Society, Faraday Transactions* **93**, 629 (1997).
- 27 N. F. Mott and M. J. Littleton, *Transactions of the Faraday Society* **34**, 485 (1938).
- 28 G. Kresse and J. Furthmüller, *Physical Review B* **54**, 11169 (1996).
- 29 G. Kresse and D. Joubert, *Physical Review B* **59**, 1758 (1999).
- 30 H. J. Monkhorst and J. D. Pack, *Physical Review B* **13**, 5188 (1976).
- 31 J. P. Perdew, K. Burke, and M. Ernzerhof, *Physical Review Letters* **77**, 3865 (1996).
- 32 W. H. Press, S. A. Teukolsky, W. T. Vetterling, and B. P. Flannery, *Numerical recipes in C (2nd ed.): the art of scientific computing* (Cambridge University Press, 1992).
- 33 S. Grimme, J. Antony, S. Ehrlich, and H. Krieg, *The Journal of Chemical Physics* **132**, 154104 (2010).
- 34 P. Varotsos, *Journal of Applied Physics* **101**, 123503 (2007).
- 35 P. Varotsos and K. Alexopoulos, *Journal of Physics and Chemistry of Solids* **38**, 997 (1977).
- 36 P. Varotsos and K. Alexopoulos, *Journal of Physics and Chemistry of Solids* **41**, 443 (1980).
- 37 A. Chroneos and R. V. Vovk, *Solid State Ionics* **274**, 1 (2015).
- 38 M. W. D. Cooper, R. W. Grimes, M. E. Fitzpatrick, and A. Chroneos, *Solid State Ionics* **282**, 26 (2015).
- 39 L. Z. Reznitsky, E. V. Sklyarov, Z. F. Ushchapovskaya, *Proc. Russ. Mineral. Soc.* **1995**, 124, 91–98.
- 40 F. A. Kröger and H. J. Vink, in *Solid State Physics*, edited by F. Seitz and D. Turnbull (Academic Press, 1956), Vol. 3, p. 307.
- 41 A. Nyttén, A. Abouimrane, M. Armand, T. Gustafsson, and J. O. Thomas, *Electrochemistry Communications* **7**, 156 (2005).
- 42 D. Enslin, M. Stjernerahl, A. Nyttén, T. Gustafsson, and J. O. Thomas, *Journal of Materials Chemistry* **19**, 82 (2009).
- 43 V. V. Politaev, A. A. Petrenko, V. B. Nalbandyan, B. S. Medvedev, and E. S. Shvetsova, *Journal of Solid State Chemistry* **180**, 1045 (2007).
- 44 M. Kempaiah Devaraju, Q. Duc Truong, H. Hyodo, Y. Sasaki, and I. Honma, *Scientific Reports* **5**, 11041 (2015).

- 45 A. R. Armstrong, N. Kuganathan, M. S. Islam, and P. G. Bruce, *Journal of the American Chemical Society* **133**,  
13031 (2011).
- 46 N. Kuganathan and M. S. Islam, *Chemistry of Materials* **21**, 5196 (2009).
- 47 C. A. J. Fisher, N. Kuganathan, and M. S. Islam, *Journal of Materials Chemistry A* **1**, 4207 (2013).
- 48 J. Heath, H. Chen, and M. S. Islam, *Journal of Materials Chemistry A* **5**, 13161 (2017).
- 49 C. Tealdi, M. Saiful Islam, L. Malavasi, and G. Flor, *Journal of Solid State Chemistry* **177**, 4359 (2004).
- 50 J. Wu, G. Gao, G. Wu, L. Liu, J. Ma, and Y. Chen, *Physical Chemistry Chemical Physics* **21**, 4947 (2019).
- 51 T. Chen, G. Sai Gautam, W. Huang, and G. Ceder, *Chemistry of Materials* **30**, 153 (2018).
- 52 P. Canepa, et al., *Nature Communications* **8**, 1759 (2017).
- 53 H. Mamiya, M. Onoda, T. Furubayashi, J. Tang, and I. Nakatani, *Journal of Applied Physics* **81**, 5289 (1997).
- 54 S. K. Pandey, *Physical Review B* **84**, 094407 (2011).
- 55 A. Chroneos, *Applied Physics Reviews* **3**, 041304 (2017).
- 56 V. Saltas, D. Horlait, E. N. Sgourou, F. Vallianatos, and A. Chroneos, *Applied Physics Reviews* **4**, 041301  
(2017).

**Table 1.** Comparison between experimental and calculated structural parameters for cubic spinel-  $\text{MgV}_2\text{O}_4$ .

Parameter	Calculated		Experiment [39]	$ \Delta $ (%)	
	Force field	DFT		Force field	DFT
$a = b = c$ ( $\text{\AA}$ )	8.3669	8.4010	8.3850	0.22	0.19
$\alpha = \beta = \gamma$ ( $^\circ$ )	90.00	90.00	90.00	0.00	0.00
$V$ ( $\text{\AA}^3$ )	585.7278	592.9295	589.5344	0.65	0.58

**Table 2.** Intrinsic defect energies calculated in  $\text{MgV}_2\text{O}_4$ .

<b>Defect process</b>	<b>Defect energy (eV)</b>	<b>Defect energy (eV)/defect</b>
Mg Frenkel/1	10.46	5.23
V Frenkel/2	13.96	6.98
O Frenkel/3	12.52	6.26
Schottky/4	37.31	5.33
MgO Schottky/5	10.26	5.13
$\text{V}_2\text{O}_3$ Schottky/6	26.80	5.36
Mg/V anti-site (isolated)/7	1.68	0.84
Mg/V anti-site (cluster)/8	1.06	0.53

**Table 3.** Activation energy calculated for Mg-ion migration in electrode materials.

<b>Material</b>	<b>Activation energy (eV)</b>
MgFeSiO <sub>4</sub>	0.60 [48]
MgTiO <sub>3</sub>	0.88 [21]
Mg <sub>6</sub> MnO <sub>8</sub>	0.82 [22]
MgTa <sub>2</sub> O <sub>6</sub>	2.21 [49]
MgVPO <sub>4</sub> O	0.58 [50]
MgCr <sub>2</sub> O <sub>4</sub>	0.69 [51]

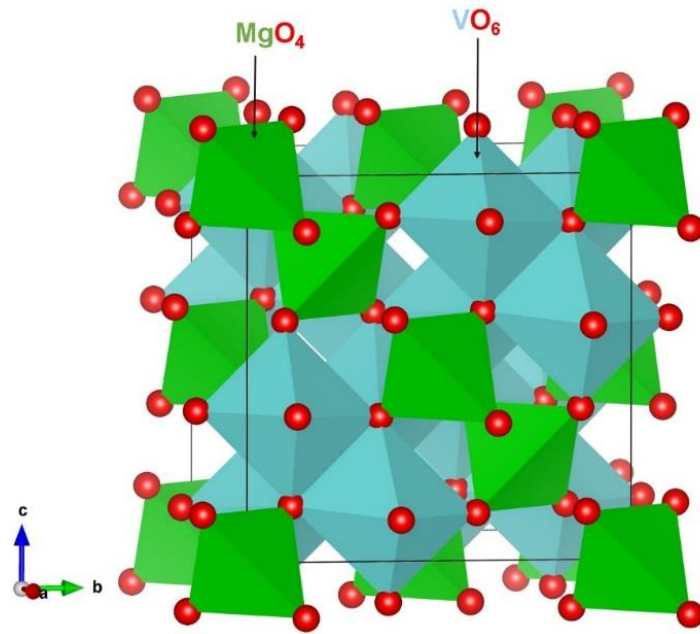


**Figure 1.** Crystal structure of spinel-MgV<sub>2</sub>O<sub>4</sub>

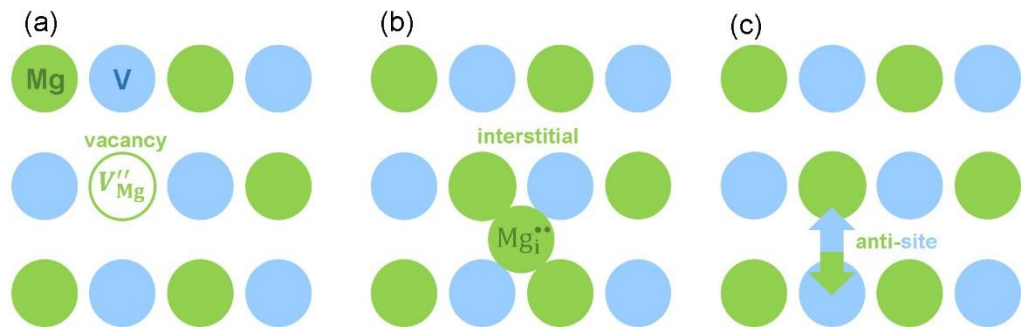


**Figure 2.** Schematic diagrams showing (a) vacancy, (b) interstitial and (c) anti-site defect

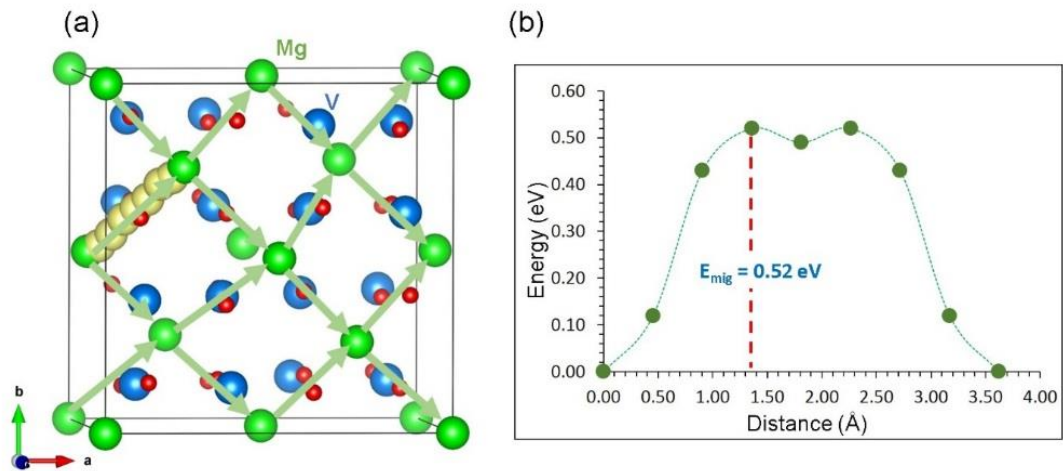


**Figure 3** (a) Mg ion diffusion paths constructed by connecting Mg hops with the Mg-Mg separation of 3.62 Å in MgV<sub>2</sub>O<sub>4</sub> and (b) energy profile diagram for the Mg hop.

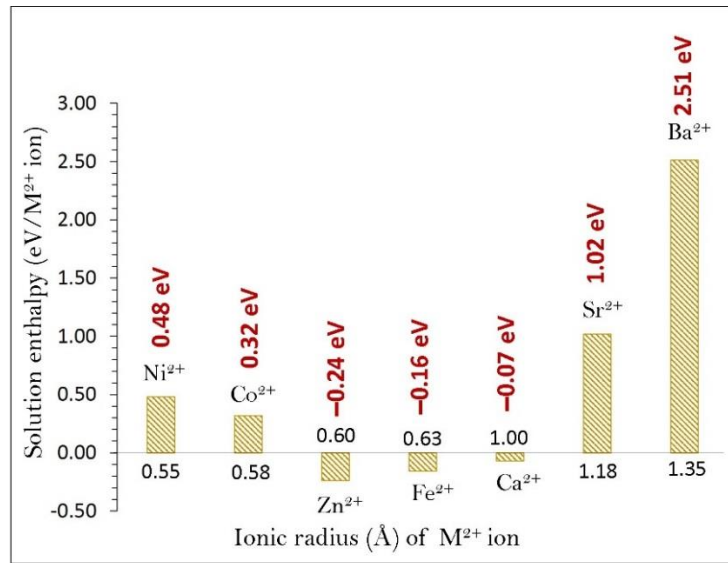


**Figure 4.** Solution enthalpies calculated for a range divalent dopants with different ion sizes at the Mg site

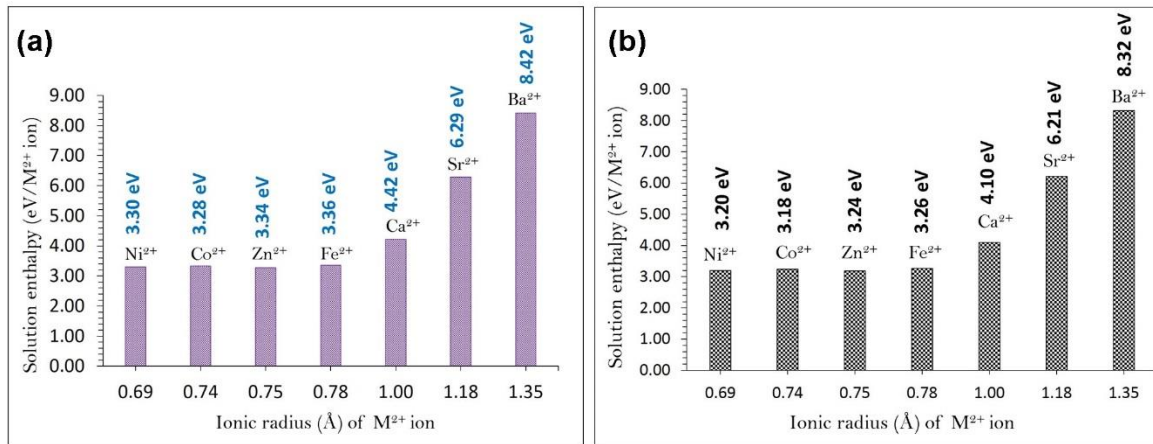


**Figure 5.** Solution enthalpies calculated for a range divalent dopants at the V site with the formation of (a) Mg interstitials and (b) oxygen vacancies.

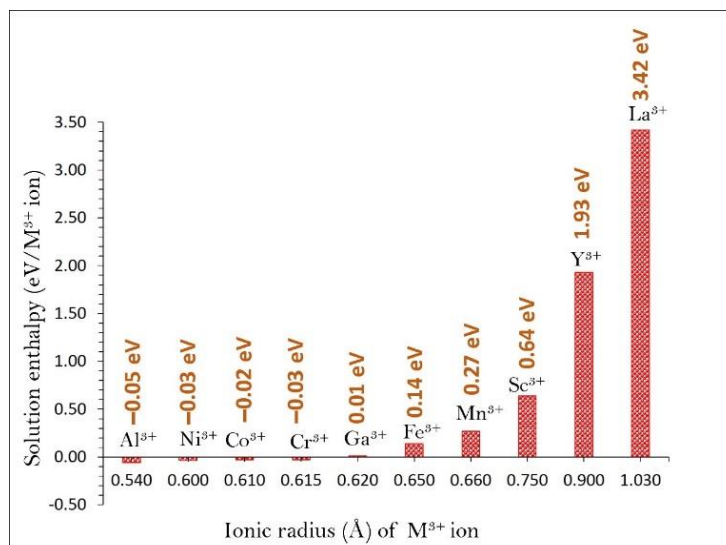


**Figure 6.** Enthalpy of solution of  $R_2O_3$  ( $R=Al, Ni, Co, Cr, Ga, Fe, Mn, Sc, Y$  and  $La$ ) as a function of  $R^{3+}$  ionic radius in  $MgV_2O_4$ .

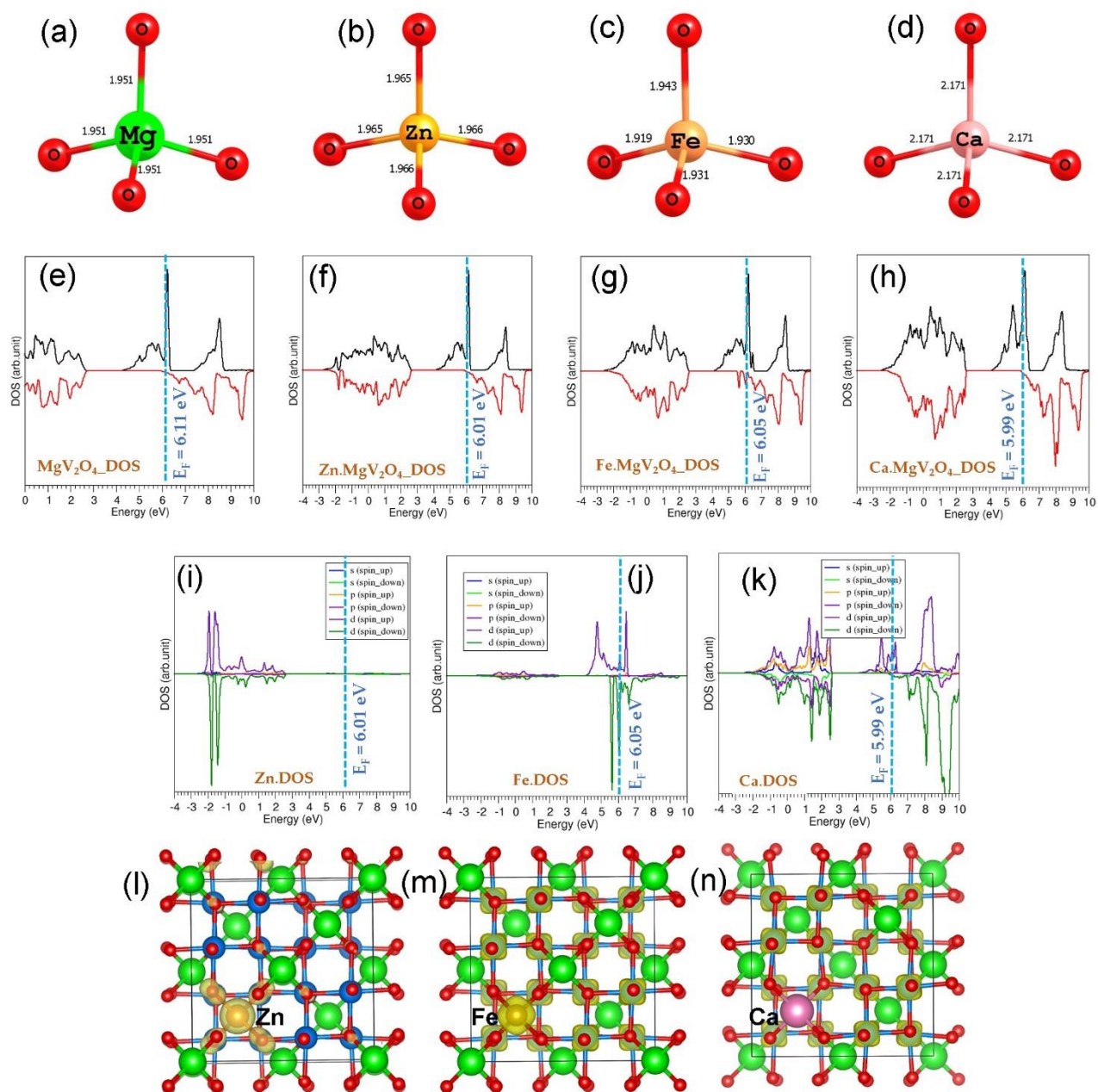


**Figure 7.** (a-d) Tetrahedral units showing bond lengths in un-doped and doped (Zn, Fe and Ca) configurations, (e-h) total DOSs (i-k) atomic DOSs and (l-n) charge density plots around the doped atoms.

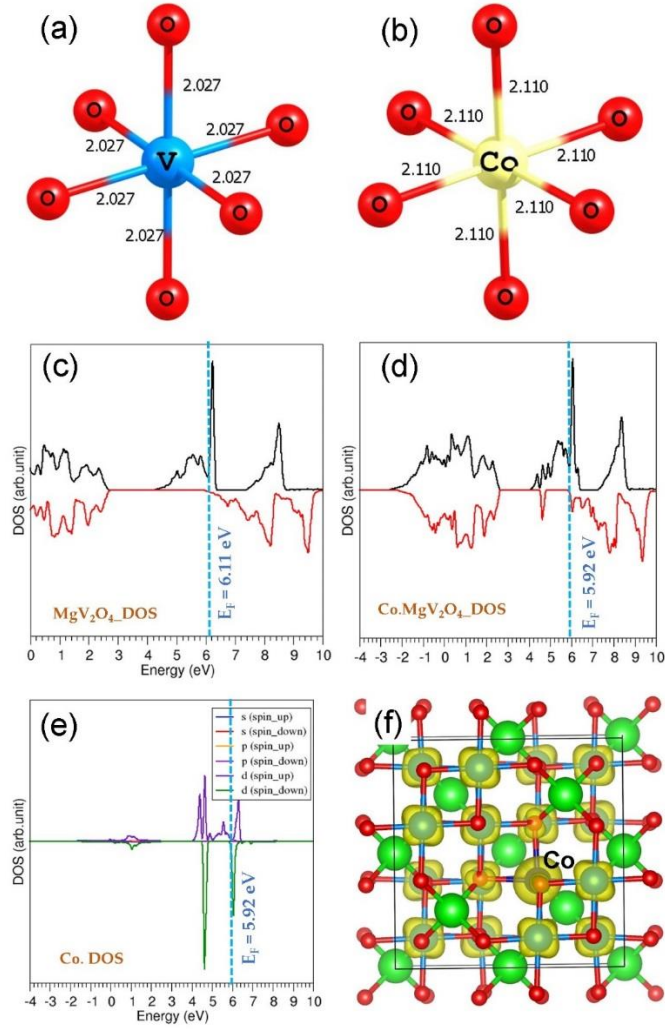


**Figure 8.** (a)  $\text{VO}_6$  octahedral unit in the relaxed defect free  $\text{MgV}_2\text{O}_4$  bulk structure, (b)  $\text{CoO}_6$  octahedral unit in the  $\text{Co}^{2+}$  doped at the V site configuration, (c) total DOS of  $\text{MgV}_2\text{O}_4$ , (d) total DOS of Co-doped configuration, (e) atomic DOS of Co and (f) constant charge density plot associated with the Co atom and an electron.

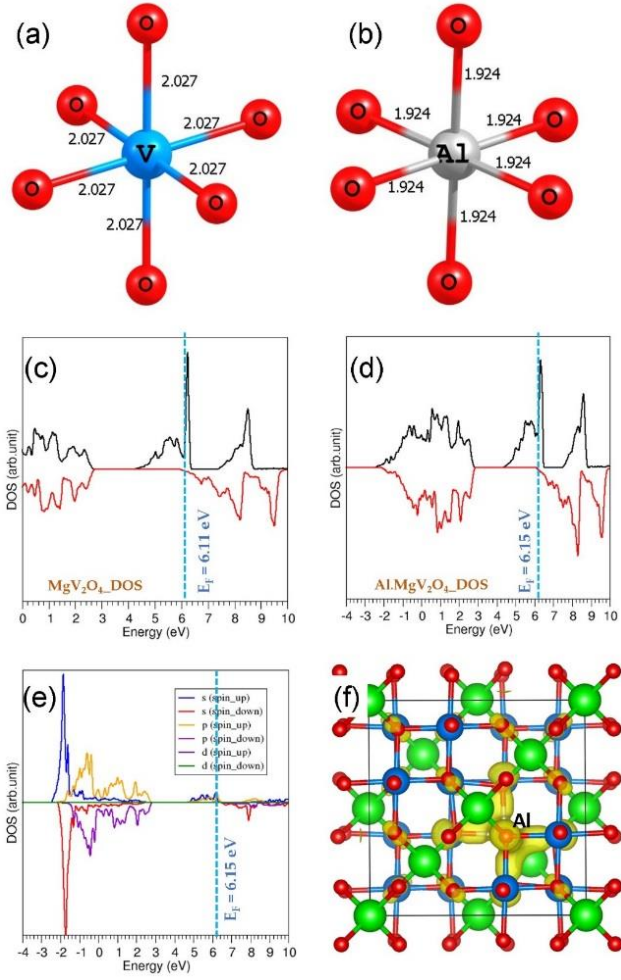


**Figure 9.** (a)  $\text{VO}_6$  octahedral unit in the relaxed defect free  $\text{MgV}_2\text{O}_4$  bulk structure, (b)  $\text{AlO}_6$  octahedral unit in the  $\text{Al}^{3+}$  doped at the V site configuration, (c) total DOS of  $\text{MgV}_2\text{O}_4$ , (d) total DOS of Al-doped configuration, (e) atomic DOS of Al and (f) constant charge density plot associated with the Al atom.